
Article:
Zhang, J., Kan, B., Pearson, A. et al. (12 more authors) (2018) Efficient non-fullerene organic solar cells employing sequentially deposited donor-acceptor layers. Journal of Materials Chemistry A, 6 (37). pp. 18225-18233. ISSN 2050-7488

https://doi.org/10.1039/C8TA06860G

Efficient Non-fullerene Organic Solar Cells Employing Sequentially Deposited Donor-Acceptor Layers

Jiangbin Zhang[1,2#], Bin Kan[3#], Andrew J. Pearson[1], Andrew J. Parnell[4], Jos Cooper[5], Xiao-Ke Liu[1,6], Patrick Conaghan[1], Thomas Hopper[2], Yutian Wu[1], Xiangjian Wan[3], Feng Gao[6], Neil C. Greenham[1], Artem A. Bakulin[2], Yongsheng Chen[3], Richard H. Friend[1*]*

[1] Cavendish Laboratory, University of Cambridge, JJ Thomson Avenue, Cambridge CB3 0HE, United Kingdom;

[2] Department of Chemistry, Imperial College London, London SW7 2AZ, United Kingdom;

[3] The Centre of Nanoscale Science and Technology and Key Laboratory of Functional Polymer Materials, State Key Laboratory and Institute of Elemento-Organic Chemistry, College of Chemistry, Nankai University, Tianjin, 300071, China;

[4] Department of Physics & Astronomy, The University of Sheffield, Hicks Building, Hounsfield Road, Sheffield S3 7RH, United Kingdom;

[5] ISIS Neutron and Muon Source, Science and Technology Facilities Council, Rutherford Appleton Laboratory, Didcot, OX11 0QX, United Kingdom;

[6] Department of Physics, Chemistry and Biology (IFM), Linköping University, Linköping SE-58183, Sweden.

[*] yschen99@nankai.edu.cn; rhf10@cam.ac.uk;

Abstract

Non-fullerene acceptors (NFAs) have recently outperformed their fullerene counterparts in binary bulk-heterojunction (BHJ) organic solar cells (OSCs). Further development of NFA OSCs may benefit other novel OSC device structures that alter or extend the standard BHJ concept. Here, we report such a new processing route that forms a BHJ-like morphology between sequentially processed polymer donor and NFA with high power conversion efficiencies in excess of 10%. Both devices show similar charge generation and recombination behaviours, supporting formation of similar BHJ active layers. We correlate the ~30 meV smaller open-circuit voltage in sq-BHJ devices to more substantial non-radiative recombination by voltage loss analysis. We also determine the exciton diffusion length of benchmark polymer PBDB-T to be 10 ± 3 nm. Our results demonstrate high-efficiency OSC devices using sequential deposition method and provide new opportunities to further improve performance of state-of-the-art OSCs.

Keywords: organic solar cells, non-fullerene acceptor, bulk heterojunction, sequential deposition, non-radiative recombination, trap states;

Introduction

Organic solar cells (OSCs) retain their flexibility and processability over large areas at relatively low cost, and have clear potential for assimilation into emerging technologies, such as building-integrated photovoltaics and wearable electronics.[1,2] The active layers of OSCs typically incorporate a heterojunction between electron donor (D) and electron acceptor (A) organic semiconductors to facilitate efficient photocurrent generation. This concept, first introduced by Tang in 1986 using a planar heterojunction (PHJ) active layer architecture,[3] was modified in 1995 toward bulk-heterojunction (BHJ) layers that overcome clear limitations of the PHJ approach. Specifically, the mismatch between absorption depth and D:A interfacial area in a PHJ device results in a low efficiency for harvesting photogenerated excitons. By forcing a phase separation length scale between D and A that is commensurate with the exciton diffusion length (10-20 nm), BHJs enable much higher quantum efficiencies and overall power conversion efficiencies (PCEs).[4,5] Since the introduction of the BHJ concept, morphological control of BHJs (e.g. D:A ratio, active layer processing conditions) has remained a key factor in the development of high-efficiency OSCs[6–12], despite the fact that a detailed mechanistic understanding of it remains under-developed.[13–16]

As an alternative to co-depositing D and A semiconductors to form a BHJ, a two-step solution deposition process can be used, wherein the electron acceptor layer (usually based on a fullerene derivative small molecule) is deposited onto the electron donor layer (usually a polymer). This structure, termed a sequentially deposited BHJ (sq-BHJ), has been used in fullerene-based OSCs, sometimes yielding quantum efficiencies comparable to an as-cast BHJ (c-BHJ) based on D:A co-deposition.[17,18,27–30,19–26] For example, the state-of-the-art sq-BHJ OSCs based on poly[4,8-bis(5-(2-ethylhexyl)thiophen-2-yl)benzo[1,2-b;4,5-b']dithiophene-2,6-diyl-alt-(4-(2-ethylhexyl)-3-fluorothieno[3,4-b]thiophene-)-2-carboxylate-2-6-diyl)] (PTB7-Th) and [6,6]-Phenyl-C71-butyric acid methyl ester ($PC_{71}BM$) show maximum PCEs of 8.6%.[17] Compared to the c-BHJ approach, sq-BHJ OSCs potentially offer several advantages from the perspective of device fabrication, namely: (i) individual layer properties such as thickness and crystallinity can be independently controlled, thereby simplifying BHJ morphology optimisation. (ii) As a consequence of (i), OSCs can be fabricated with high reproducibility. (iii) The morphology of a sq-BHJ layer might be closer to thermal equilibrium and therefore more stable under conventional OSC operating temperatures.

With fullerene-based semiconductors remaining the archetypal electron acceptor for OSCs, the recent fast advancement of high-performance non-fullerene acceptors (NFAs) has motivated a careful evaluation of the future direction of OSC research.[31–35] Beginning in 2015, the PCEs of champion NFA-based single-junction OSCs have been higher than those fabricated using fullerenes, and now stands at an impressive 14%.[36–45] Following this progress, the performance of OSCs based on other types of active layer architectures, such as ternary-blend OSCs[46–49], tandem-junction OSCs[50–53] and semitransparent OSCs[54–56], have all benefited from substitution of a fullerene-based electron acceptor for a NFA.

In this contribution, we report an efficient sq-BHJ device using poly[(2,6-(4,8-bis(5-(2-ethylhexyl)thiophen-2-yl)-benzo[1,2-b:4,5-b']dithiophene))-alt-(5,5-(1',3'-di-2-thienyl-5',7'-bis(2-ethylhexyl)benzo[1',2'-c:4',5'-c']dithiophene-4,8-dione)] (PBDB-T) as the donor and NCBDT as the acceptor. Optimised sq-BHJ layers are prepared using dichloromethane (DCM) as the solvent for NFA without post-treatments or solvent additives. The resultant OSCs show >10% PCE, comparable to that achieved by OSCs based on as-cast BHJ layers. This efficiency is one of the highest reported for sq-BHJ OSCs. As PBDB-T remains a benchmark polymer for NFA OSCs, we also determined its exciton diffusion length to be 10 ± 3 nm from external quantum efficiency (EQE) measurements. To understand the performance of both sq-BHJ and c-BHJ OSCs we characterise the factors governing voltage loss using stead-state and time-resolved optical and electrical measurements.

Results and Discussion

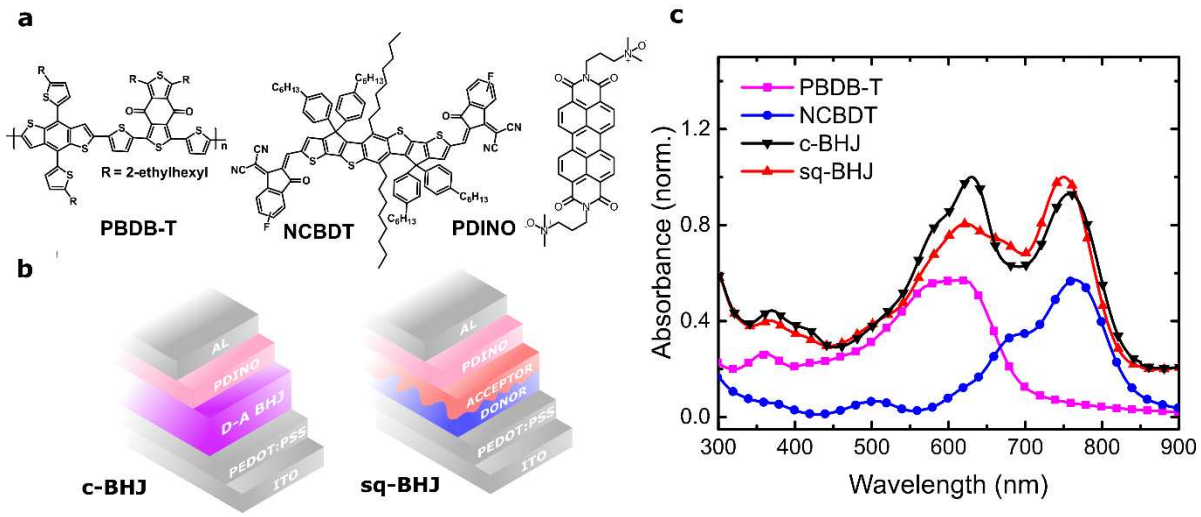

Figure 1. (a) Chemical structures of PBDB-T (donor), NCBDT (acceptor) and PDINO (electron-transport layer). (b) Device structures where the photoactive layer is based on a c-BHJ or sq-BHJ architecture. (c) Absorption spectra of pristine PBDBT and NCBDT films.

OPV materials and devices. Fig. 1a presents the chemical structures of the electron donor (PBDB-T), electron acceptor (NCBDT) and electron transport layer (PDINO, perylene diimide functionalized with amino N-oxide). PBDB-T is widely used as a benchmark electron donor for blending with emerging electron acceptors.[57] The central electron-donating BDT unit has also featured in many ladder-type NFAs[58], such as NCBDT in this study. [59] The device structure in this study, shown in **Fig. 1b**, is ITO/PEDOT:PSS (poly(3,4-ethylenedioxythiophene) polystyrene sulfonate), ~30 nm)/active layer/PDINO (~5 nm)/Al (100 nm). For the sq-BHJ film, the donor layer was deposited from solution in chloroform, and the upper acceptor layer was cast from DCM solution. For the bulk-BHJ devices, the donor and acceptor mixed layer was deposited from chloroform. PDINO was then spin-coated from methanol solution on the active layers, followed with an evaporated Al layer. To simplify device fabrication, we do not subject either active layer architecture to any post-film deposition annealing. As shown in our previous study, the peak optical absorption of NCBDT shifts from ~730 nm in dilute solution to ~760 nm in an as-cast film, suggesting ordered molecular packing in the solid state.[59] **Fig. 1c** shows the complementary absorption of the pristine materials across the visible and near-IR region together with the absorption spectra of c-BHJ and sq-BHJ blends.

Table 1. Characteristics of the c-BHJ and sq-BHJ devices.

Active layer layout	V_{OC} (V)	J_{SC} (mA cm^{-2})	FF	PCE (%)	J_{SC} (EQE) (mA cm^{-2})	Hole mobility ($\times 10^{-4}$ m^2 V^{-1} s^{-1})	Electron mobility ($\times 10^{-4}$ m^2 V^{-1} s^{-1})
c-BHJ	0.847 (0.842±0.003)	18.64 (18.32±0.20)	64.6 (63.5±0.5)	10.19 (10.05±0.12)	18.65	1.28 (1.21±0.04)	1.18 (1.09±0.05)
sq-BHJ	0.824 (0.820±0.003)	19.45 (19.14±0.15)	62.9 (61.8±0.6)	10.04 (9.70±0.24)	19.30	0.88 (0.81±0.05)	0.92 (0.85±0.07)

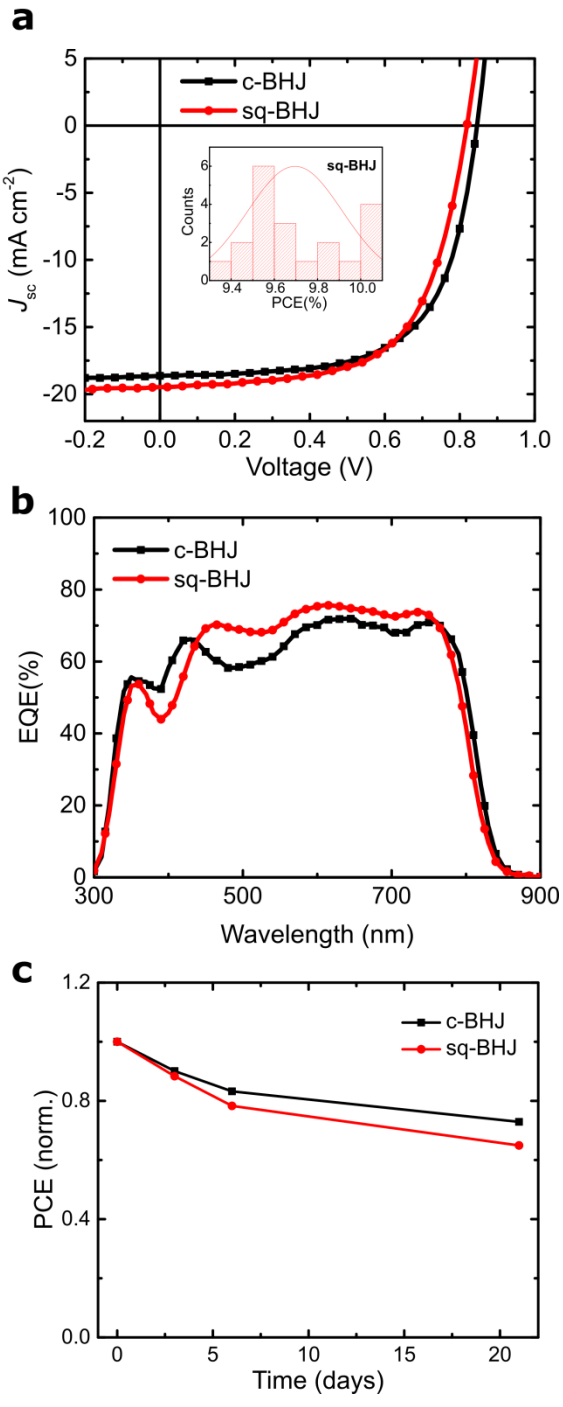

Figure 2. (a) Current-density voltage measurements under one-sun illumination. Inset: the distribution of PCE in 20 sq-BHJ devices. (b) Spectral dependence of the EQE. (c) Device efficiency change over 3 weeks under nitrogen atmosphere.

Solar cell performance. C-BHJ OSCs with an active layer thickness of 100 ± 5 nm show a PCE of ~10%, reproducing the results from our previous study.[59] Optimisation of the sq-BHJ OSCs considered the following processing variables: PBDB-T and NCBDT solution concentration, film deposition spin-speed, and casting solvent, the outcomes of which are tabulated in **Table S1-3**. From this exercise, devices with PCE of ~10% were also obtained. We note that during the preparation of manuscript, Hou et al., reported devices with ~13% PCE using this processing method.[60] Here, the nominal thicknesses of the donor and acceptor layer were 45 ± 5 and 50 ± 5 nm, respectively, and the total active layer thickness was 90 ± 5 nm. Data presented in **Figure 2** shows the overall photovoltaic behaviour for both c-BHJ and sq-BHJ OSCs with related performance metrics summarized in **Table 1**. Compared with the c-BHJ OSCs, sq-BHJ OSCs have larger short-circuit current density (J_{SC}) up to 19.45 mA cm^{-2}, which likely results from optimised vertical stratification.[28] The larger open-circuit voltage (V_{OC}) of the c-BHJ OSCs has previously been observed in a polymer:fullerene OSC, but the origin of this difference was not investigated in detail.[19] The fill factor (FF) for the sq-BHJ OSCs, was found to be relatively more sensitive to the thicknesses of the donor and acceptor layers (**Table S2-3**), which may reflect a greater imbalance between electron and hole mobilities, and/or enhanced bimolecular recombination (BR). We measured the dark current density-voltage behaviour of single carrier devices in the space-charge limited current regime to determine respective charge carrier mobilities (**Figure S1**). From this experiment, the electron and hole mobilities were found to be smaller in the sq-BHJ devices than those in c-BHJ devices, consistent with the FF values found for the corresponding OSCs. Fullerene-based OSCs are not photo-stable mainly due to sensitivity of fullerene to environment. Sq-BHJ devices often show an improved stability over c-BHJ devices in fullerene-based OSCs. The efficiency increase in NFA OSCs also accompanies its improved device in c-BHJ devices probably due to elimination of fullerene derivatives. In such scenario, the device stability of NFA-based sq-BHJ devices is not reported yet. **Fig. 2c** shows that sq-BHJ devices preserve 65% of its original efficiency after 3 weeks while c-BHJ devices maintain 72%. The other photovoltaic parameters are shown in **Figure S2** and the full dataset is included in **Table S4**. We find that the efficiency drop is mainly due to decreased J_{SC} while V_{OC} and FF degraded similarly. The inferior stability of sq-BHJ devices might be due to its not thermally stabilized interfacial morphology, and or trap states at the interface.

Charge generation and recombination characterised with steady-state techniques. Fig. 2b shows the EQE spectra for both OSC types. Between 450 and 800 nm, the EQE for the sq-BHJ OSC is higher and more uniform than that for the c-BHJ OSC, which contains a clear local minimum around 500 nm. This dip in EQE may be due to lower absorption efficiency of the c-BHJ layer and/or suboptimal optical management of the device stack. We note, however, that the sq-BHJ layer is more likely to exhibit vertical heterogeneity, and the photocurrent generation efficiency could therefore exhibit a greater dependence on position within the OSC stack.[61] This optical management factor can be understood by substantially increasing the PBDB-T layer thickness. Data presented in **Figure S3** shows that the EQE at long wavelengths (>600 nm) becomes lower as a result. Alongside improved semiconductor design, future device optimisation should carefully consider the distribution of materials within a sq-BHJ layer in order to accurately predict the device structure which enables maximal EQE.[28] We also measured the dependence of photocurrent density on effective bias (V_{eff}, defined as the applied bias minus the built-in voltage of the OSC) and light-intensity dependence of J_{SC} and V_{OC}. Each of these measurements does not show significant differences between these device types (**Figure S4-5**), supporting the notion of similar charge generation and recombination in both OSCs.

Table 2. Determination of non-radiative and radiative energy loss in c-BHJ and sq-BHJ devices.

Active layer layout	E_{gap} (±0.01)	qV_{OC} (±0.005)	$q\Delta V$	$\Delta E_1 = E_{gap} - qV_{OC}^{SQ}$	$\Delta E_2 = qV_{OC}^{SQ} - qV_{OC}^{rad}$	$\Delta E_3 = qV_{OC}^{rad} - qV_{OC}$	EQE_{EL} (exp.)[1]	$q\Delta V_{OC}^{non-rad,exp}$ (V)
c-BHJ	1.54	0.847	0.693	0.282	0.038	0.373	9.1×10^{-7}	0.347
sq-BHJ	1.54	0.824	0.716	0.281	0.033	0.402	2.2×10^{-7}	0.383

1 The EQE_{EL} was determined at the injection current of 155 mA cm^{-2}. In the table, q is the element charge, ΔV is the voltage loss, E_{gap} is the lower bandgap of D or A, V_{OC}^{SQ} is the maximal voltage by the Shockley-Queisser limit, V_{OC}^{rad} is the open-circuit voltage when there is only radiative recombination. EQE_{EL} is the radiative quantum efficiency of the solar cell when charge carriers are injected into the device in the dark. $\Delta V_{OC}^{non-rad,exp}$ is the voltage loss calculated from EQE_{EL}.

Characterisation of energy loss. Within the literature, state-of-the-art NFA-based OSCs exhibit a much lower voltage loss compared to state-of-the-art fullerene-based OSCs, overcoming the traditionally severe trade-off between high J_{SC} and high V_{OC}. This is primarily due to their high charge generation efficiency despite the minimal driving force for exciton dissociation, in addition to their much improved electroluminescence (EL) efficiency.

These characteristics motivate us to reflect on the larger V_{OC} (by ~23 meV) of the c-BHJ OSCs compared to the sq-BHJ OSCs, and to characterize the detailed energy losses in both devices. As discussed by Nelson[62] and Yan[63], energy loss can be separated into three categories: 1) $\Delta E_1 = E_{\mathrm{gap}} - \mathrm{q}V_{\mathrm{OC}}^{\mathrm{SQ}}$, mainly radiative recombination due to the absorption above the bandgap; 2) $\Delta E_2 = \mathrm{q}V_{\mathrm{OC}}^{\mathrm{SQ}} - \mathrm{q}V_{\mathrm{OC}}^{\mathrm{rad}}$, due to additional radiative recombination from the absorption below the bandgap; 3) $\Delta E_3 = qV_{\mathrm{OC}}^{\mathrm{rad}} - qV_{\mathrm{OC}} \approx -kT \ln \mathrm{EQE}_{\mathrm{EL}}$ from the non-radiative recombination. The bandgap of NCBDT is ~1.54 eV, determined by the cross point of the absorption and emission spectra (**Figure S6**).[32] With the same material combination and similar EQE in both structures, there is only a small difference in the energy loss from ΔE_1 (1 meV) and ΔE_2 (5 meV) as determined by EQE spectra. Thus, the dominant loss channel should be non-radiative recombination, estimated to be ~29 meV. This parameter is fundamentally connected with the EL efficiency. We directly measured EQE_{EL} by recording the EL intensity from both OSCs under forward bias conditions (**Figure S7**). The ratio of EL (**Table 2**) efficiencies corresponds to a voltage difference of ~36 meV, which is comparable with the predicted ΔE_3 of ~29 meV. This is also reflected by the measured dark current density-voltage behaviour, which inversely correlates with EL efficiency (**Figure S8**).

For poly(3-hexylthiophene-2,5-diyl) (P3HT):[6,6]-phenyl-C61-butyric acid methyl ester ($PC_{61}BM$) OSCs reported elsewhere, an identical V_{OC} was obtained using sq-BHJ and c-BHJ active layers (with thermal annealing treatment).[23] However, polymer:fullerene OSCs utilising poly[N-9'-heptadecanyl-2,7-carbazole-alt-5,5-(4',7'-di-2-thienyl-2',1',3'-benzothiadiazole)] (PCDTBT) demonstrated a higher V_{OC} in sq-BHJ devices.[22] Thus the voltage output depends on material combination and post-treatment, both of which strongly influence the D:A interfacial morphology. In our work, V_{OC} in the sq-BHJ OSCs studied here is smaller than that in the c-BHJ devices, which can be explained by higher non-radiative recombination.

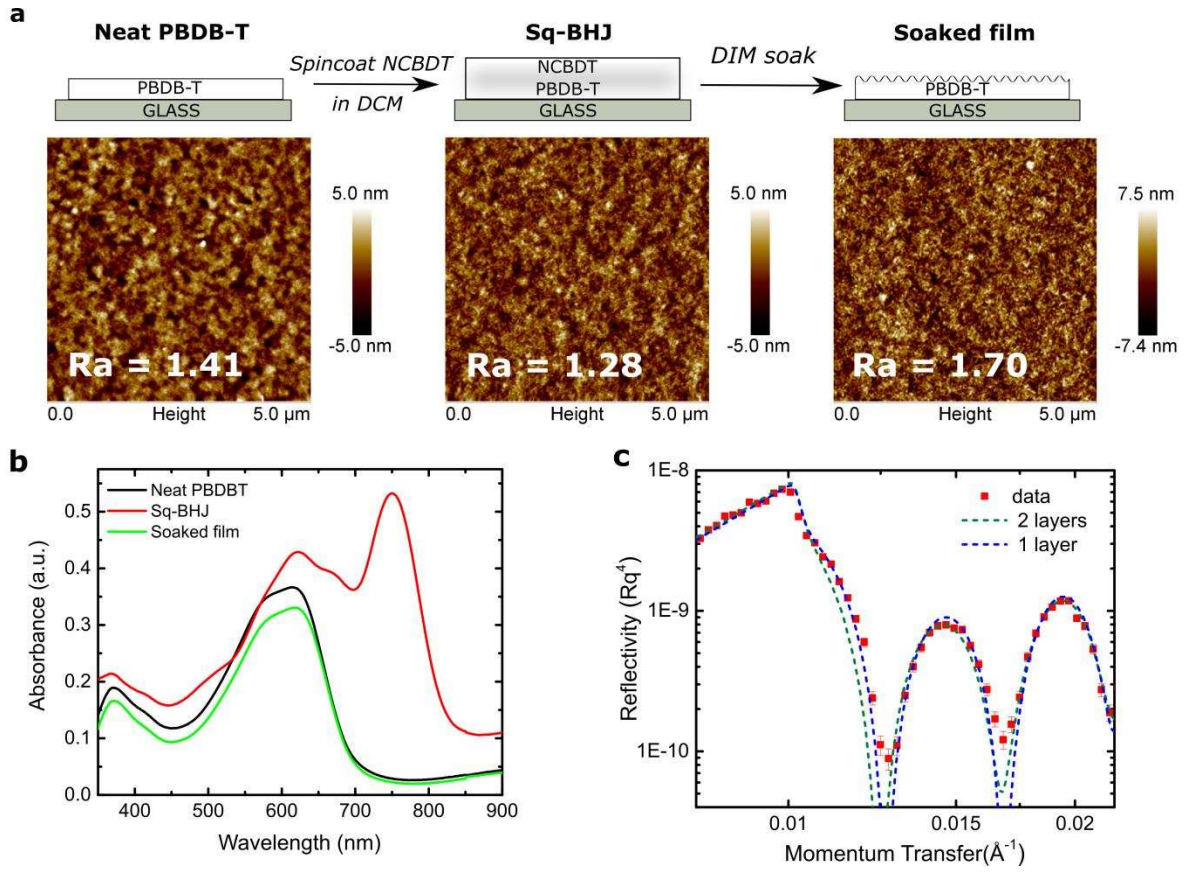

Figure 3. Morphological characterisation of PBDB-T and PBDB-T:NCBDT blend films. (a) AFM images showing the surface nanostructure of pristine PBDB-T layer, and a PBDB-T:NCBDT sq-BHJ before and after NCBDT removal. Here the NFA was washed from the sample using DIM solvent (b) Absorption spectra corresponding to samples in (a). (c) Measured and simulated neutron reflectivity data of a sq-BHJ film, with simulated data considering either a homogeneous PBDB-T:NCBDT blend layer or strict PBDBT:NCBDT bilayer.

Morphological characterisation. To realise efficient sq-BHJ OSCs, a processing solvent with partial solubility for the bottom layer and good solubility for the top layer is required. Dichloromethane (DCM) meets these criteria as it only partially dissolves PBDB-T, in contrast to tetrahydrofuran (THF) which washes away the polymer layer entirely (**Figure S9**). This contrasts with the results of Kim et al. on PTB7 films, where it was found that DCM washed away 90% of material, mostly likely regions of relatively low molecular weight and high disorder.[29] Scanning probe microscopy images in **Fig. 3a** show the evolution of the PBDB-T film surface structure during these processing steps. Following diiodomethane (DIM) washing, NCBDT is successfully removed as inferred from UV-Vis measurements (**Fig. 3b**). The reduction in PBDB-T absorption results from the process of NCBDT deposition and its exposure to DCM solvent as DIM is an orthogonal solvent to PBDB-T (**Figure S10**). We note that DIM is toxic and reactive and should not be used for device

fabrication. The resultant increase in PBDB-T surface roughness (to 1.70 nm) indicates that polymer reorganisation can take place during second layer deposition, which likely encourages intermixing between PBDB-T and NCBDT. Data obtained using neutron reflectivity (**Fig. 3c** and **Figure S11**) is fitted to a model that implies uniform mixing of sq-BHJ film rather than a strict bilayer structure. However, as the small difference in scattering length densities between PBDB-T and NCBDT (~0.2×10^{-6} $Å^{-2}$) places a relatively large uncertainty on any model output, we are not able to determine the gradient in NCBDT distribution using this data. More advanced characterization techniques are required to precisely image the vertical heterogeneity of the BHJ active layer.

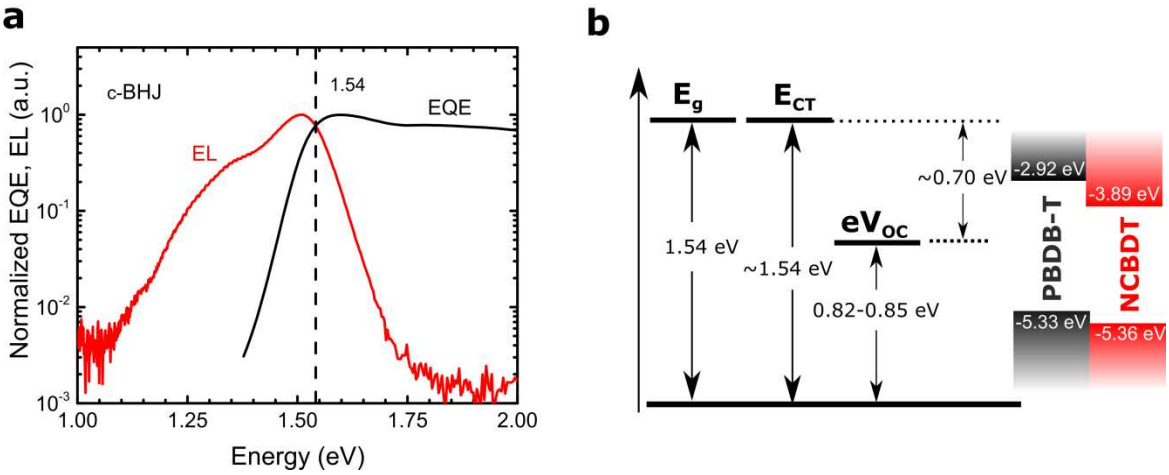

Figure 4. (a) EL and EQE profile for determination of bandgap of possible interfacial states. (b) Left: the energy level of the optical bandgap and possible charge-transfer (CT) states (1.54 eV) with a device V_{OC} around 0.82-0.85 V and recombination energy loss of ~0.70 eV; Right: highest occupied molecular orbital (HOMO) and lowest unoccupied molecular orbital (LUMO) energy levels of PBDB-T and NCBDT.

D-A interfacial energetics. We naturally question whether the differences in c-BHJ and sq-BHJ films influence the energetics inside the D:A intermixed regions. As mentioned previously, NFA OSCs often benefit from high charge generation efficiencies despite a small driving energy. In contrast, for fullerene-based OSCs, a small driving energy leads to poor charge generation efficiency.[64] From **Fig. 4b**, the energetic difference between PBDB-T and NCBDT HOMO levels is ~30 meV. However, the high peak EQE ~75% implies efficient light harvesting. Our high-performance devices thus serve as a model system for investigating D:A interface energetics in a sq-BHJ OSC that contains an A-D-A type NFA. In the EQE graph and EL emission, a Gaussian-type shoulder is usually characteristic of CT states.[65] As shown in **Fig. 4a**, it is difficult to confirm such a shoulder in the EQE and EL data. The cross point energy of EQE and EL spectra[66,67] is 1.54 eV, the same as the bandgap

of the pure acceptor (**Figure S5**). From this we conclude that there is a negligible driving force for charge transfer (**Fig. 4b**). This result agrees with measurements made on another category of NFAs based on fused aromatic diimides reported by Yan et al.[63] No change in EL and PL spectra under various biases was observed as shown in **Figure S12-13**, which indicates that the emissive spectra are from the same species, possibly singlet excitons. This is quite different from the low energy offset (~50 meV) fullerene-based blends PIPCP:$PC_{61}BM$, where the PL intensity of the BHJ blend is field-dependent.[68] Intramolecular vibrations in CT states have been suggested to explain the intrinsic limit for the non-radiative recombination in fullerene-based OSCs, but in these novel NFA OSCs, the intrinsic limit of non-radiative recombination has not been determined. A systematic investigation of the charge generation mechanism is still missing[59], and the effect of charge delocalization and non-uniform electronegativity in strong intramolecular push-pull molecules requires further attention.[69] At this stage of our research, we do not find substantial energetic difference between the c-BHJ and the sq-BHJ OSCs despite their different preparation methods.

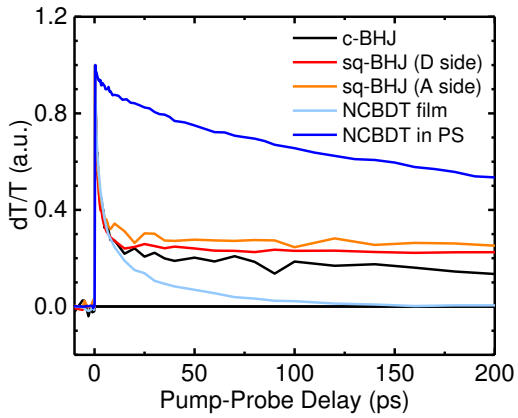

Figure 5. Kinetics from pump-probe spectroscopy with selective acceptor excitation at 800 nm. The kinetics is averaged between 1000 and 1100 nm. The sq-BHJ film was excited at two directions, either donor side first, or acceptor side first. The kinetics from the pure acceptor film and the NCBDT:PS blend film are for reference.

Transient absorption. To observe ultrafast kinetics, we used femtosecond optical spectroscopy. In the optical pump-probe measurement, we selectively excited NCBDT with 800 nm pulses. **Figure 5** shows the kinetics of the exciton peak (averaged between 1000-1100 nm)[59] extracted from the full spectra in **Figure S14**. A faster exciton decay in the D-A blend than that in the NCBDT: polysterene (PS) blend suggests efficient exciton quenching in both c-BHJ and sq-BHJ blends. Interestingly, kinetics at short timescales (< 20 ps) from D:A blends are very similar to that from pure NCBDT blend. This indicates a slow charge-transfer

rate under such low offset in HOMO energies (**Fig. 4b**).[70] The signal after 100 ps in D-A blends cannot come from excitons which are expected to decay completely (as seen in measurements on pure NCDBT film), but possibly from polarons. The smaller amplitude in c-BHJ films thus might come from faster BR due to its finer phase separation. Such fast recombination has been observed in PIPCP:PCBM blends.[71] Overall, from transient absorption measurements, there is not much difference in charge generation in c-BHJ and sq-BHJ films.

Sequentially deposited devices using different materials. To further test this sequential deposition method, we also fabricated a series of NFA-based OSC devices using a combination of several donors and acceptors (PBDB-T, PBDTTT-EFT (Poly[4,8-bis(5-(2-ethylhexyl)thiophen-2-yl)benzo[1,2-b;4,5-b']dithiophene-2,6-diyl-alt-(4-(2-ethylhexyl)-3-fluorothieno[3,4-b]thiophene-)-2-carboxylate-2-6-diyl)]), PDCBT (poly[(4,4′-bis(2-butyloctoxycarbonyl-[2,2′-bithiophene]-5,5-diyl)-alt-(2,2′-bithiophene-5,5′-diyl)]), NCBDT and ITIC (3,9-bis(2-methylene-(3-(1,1-dicyanomethylene)-indanone)-5,5,11,11-tetrakis(4-hexylphenyl)-dithieno[2,3-d:2′,3′-d′]-s-indaceno[1,2-b:5,6-b′]dithiophene)). As shown in **Table 3**, for PBDB-T and PDBTTT-EFT, the device efficiencies using c-BHJ and sq-BHJ architectures are similar, while for PDCBT, sq-BHJ device efficiencies are much lower than c-BHJ ones. This is probably due to DCM used for processing. DCM is chosen for working with PBDB-T in this work. We note that some other solvents may work better for PDCBT blends. The lower J_{SC} and FF in sq-BHJ devices may indicate an inefficient exciton dissociation and/or severe charge recombination, probably relating to not intermixed morphology and limited exciton diffusion length of organic materials. V_{OC}s of sq-BHJ devices are within 50 meV difference compared with c-BHJ ones. Overall, these device results agree with our previous discussion that the formation of BHJ-like morphology greatly depends on the properties of polymer and the solvent for the NFA layer, and various solvents may be needed to optimise a specific blend.

Table 3. Device performance comparison of c-BHJ and sq-BHJ devices based on different donor and acceptor combinations. The solvent for these devices is DCM.

Active layer	Layout	V_{OC} (V)	J_{SC} (mA cm^{-2})	$J_{SC\ EQE}$ (mA cm^{-2})	FF (%)	PCE (%)
PBDB-T:ITIC	c-BHJ	0.898 (0.899±0.02)	14.11 (14.19±0.09)	14.07	56.7 (55.0±1.2)	7.14 (7.00±0.10)
	Sq-BHJ	0.835 (0.833±0.004)	14.82 (15.08±0.16)	14.28	47.4 (45.9±0.9)	5.86 (5.77±0.09)
PBDTTT-	c-BHJ	0.781	17.39	17.17	65.6	8.92

EFT:NCBDT		(0.780±0.001)	(17.62±0.16)		(64.0±1.0)	(8.82±0.10)
	Sq-BHJ	0.759 (0.759±0.002)	17.37 (17.20±0.13)	16.92	62.8 (62.7±0.3)	8.27 (8.19±0.06)
PBDTTT-EFT:ITIC	c-BHJ	0.805 (0.807±0.001)	14.60 (14.63±0.10)	14.46	60.3 (59.5±0.6)	7.09 (7.03±0.04)
	Sq-BHJ	0.794 (0.792±0.004)	14.88 (14.70±0.14)	14.64	60.3 (59.5±0.6)	7.13 (6.97±0.15)
PDCBT:NCBDT	c-BHJ	0.872 (0.870±0.002)	12.91 (12.93±0.09)	12.46	61.3 (60.2±2.2)	6.91 (6.77±0.30)
	Sq-BHJ	0.873 (0.870±0.002)	8.39 (8.02±0.30)	-	44.7 (44.9±0.2)	3.28 (3.14±0.14)
PDCBT:ITIC	c-BHJ	0.927 (0.923±0.004)	14.15 (14.05±0.19)	14.08	64.9 (64.2±0.6)	8.51 (8.33±0.22)
	Sq-BHJ	0.905 (0.902±0.004)	5.99 (5.59±0.33)	-	43.9 (42.4±1.7)	2.38 (2.15±0.21)

Exciton diffusion length of PBDB-T. As a benchmark polymer, the exciton diffusion length of PBDB-T is still yet to be determined. We fabricated PBDB-T:C_{60} PHJ with various donor layer thicknesses (~8 nm to 60 nm, measured by spectroscopic ellipsometry). The thickness of the C_{60} layer is fixed at 60 nm to have the constructive interference at ~500 nm for the optimum device efficiency.[72] As shown in **Fig. S15b-c**, the donor thickness of ~20 nm gave the highest efficiency. According to the simple relationship,[73]

$$x_{max} = \frac{L \ln \alpha L}{\alpha L - 1}$$

where x_{max} is the distance from the electrodes (excluding PEDOT:PSS layer), L is the exciton diffusion length, α is the absorption coefficient.

The absorption coefficient of PBDB-T was determined to be 2.3×10^5 cm^{-1}. According to **Fig. S15d**, the exciton diffusion length is 10 ± 3 nm.

Outlook

BHJ morphological optimisation has been relatively well studied and optimised in the past twenty years, while there are still limited efforts on understanding the sq-BHJ devices. Here we show that sq-BHJ layout carries high potential and can demonstrate performance comparable to as-cast co-depositing BHJ without any post treatments or solvent additives. At the same time, this structure may process several technology relevant advantages compared with one-step BHJ formation for future exploration, such as i) straightforward device fabrication and optimisation; ii) control of interfacial disorder for eliminating trap states; iii) engineering of distortion of EQE spectra for higher photocurrent; iv) device with higher morphological stability. We believe that future work will make it possible to combine the

high-PCE achievement of this study with one or several outlined potential advantages and make sq-BHJ suitable for practical applications.

Experimental details.

Materials. PBDB-T was purchased from Ossila (M1002). NCBDT was synthesized using the procedure reported elsewhere.[59] Chloroform, DCM, dichloroethane (DCE) and trichloroethane (TCE) were bought from Sigma Aldrich. DIM was from Alfa Aesar.

OPV device fabrication. The device structure was glass/ITO/PEDOT:PSS/active layer/PDINO/Al. The glass substrate with ITO was cleaned sequentially by deionized water, acetone and isopropyl alcohol under ultrasonication for 10 min each. The subsequent PEDOT:PSS layer was spin-coated at 5000 RPM for 45 s, and then baked at 150 ºC for 20 min in ambient atmosphere. For the sq-BHJ film, the donor layer was deposited from 6 mg/ml solution in chloroform at 1900 RPM for 20 s, and the subsequent acceptor layer was cast from 6 mg/ml solution in DCM at 2500 RPM for 40 s. PDINO (1 mg/ml in CH_3OH) was spin-coated on the active layer at 3000 RPM for 40 s. Finally, a 100 nm Al layer was deposited under high vacuum. The effective area of each cell was 4.5 mm^2.

J-V characterisation and EQE measurements. Current-density voltage curves were measured using a Xenon lamp under the AM 1.5 solar illumination (Oriel 96000) in an argon-filled glovebox. The simulator irradiance was characterized using a calibrated spectrometer and the illumination intensity was calibrated using a silicon reference diode. EQE spectrum was measured together with a lock-in amplifier (SR 810, Stanford Research Systems).

EQE_{EL}, field-dependent PL and EL. EL emission from the device was collected by a silicon photodiode with an active area of 100 mm^2, with fixed distance between the device and the photodiode. The current-voltage characteristics of the device were measured with a Keithley 2400 source meter and the current outputs of the photodiode were measured with a Keithley 2000 source meter. Steady-state PL was measured from encapsulated films using a home-built setup with a 405 nm laser (Coherent) as the excitation source. The collected PL was focused into a spectrometer (Andor). For field-dependent PL, the encapsulated devices were connected to and biased by a source meter (Keithley 2400). With the same setup, the bias-dependent EL was measured in the injection region. A 500 nm long-pass filter was used to block the excitation scattering.

Neutron reflectivity. NR measurements of thin film layers were made using the same spin coating parameters as for the actual devices. The substrates were 5 mm thick circular silicon

wafers (Prolog Semicor, Ukraine) with diameter of 50.8 mm. The NR data was measured at the ISIS pulsed Neutron and Muon Source (Oxfordshire, UK) using the instrument OFFSPEC, which has a useable incident neutron wavelength range from 2-12 Å. A number of incident angles were collected to cover the measured momentum transfer range 0.008-0.238 $Å^{-1}$. We measured reference samples for each pure material (PEDOT:PSS, PBDB-T and NCBDT) which allowed us to unambiguously measure the scattering length density (SLD) of each layer independently. The PEDOT:PSS layer SLD, thickness and roughness were constrained in the device layer films, whilst silicon oxide thickness was allowed to vary. The NR data was modelled using the scheme of Névot and Croce[74] as a number of layers each having a roughness, thickness and a SLD. For the as-cast BHJ layer a single fit was used. For the sequentially processed layers, fitting was performed for two possible cases, that of a bilayer architecture and a single layer. In the former, the SLD of each layer was constrained to the values measured for the single layer films.

Pump-probe spectroscopy. 800 nm, ~200 fs pulses were generated by a regenerative Ti:sapphire regenerative amplifier (Spectra Physics, Solstice Ace) operating at 1 kHz. A portion of the seed pulses were directly sent into the sample area, while another portion was sent to a delay stage, followed by generation of the broadband probe pulses (~950-1350 nm). Part of the probe light was split off and used as the reference to reduce the pulse fluctuation. Both probe and reference beams were detected using a pair of linear image sensors (Hamamatsu). The signal was read out at the full laser repetition rate by a custom-built board (Stresing Entwicklungsburo). The beam size of pump and probe pulses were estimated to be ~0.5 mm^2. The sq-BHJ and c-BHJ films were prepared following the procedures for device fabrication. Pure NCBDT film was spin-coated at 3000 RPM for 40 s from a 6 mg/ml solution in CF, while the NCBDT:PS (weight ratio, 1:49) blend film was cast from chlorobenzene. The pump pulse energy was 250 nJ for NCBDT:PS film and 50 nJ for other films.

Associated Content

Supporting Information:

Hole and electron mobilities extracted from the SCLC, device stability over 3 weeks, EQE profile of the c-BHJ, and the sq-BHJ devices with different thicknesses of the PBDB-T layer, photocurrent generation versus the effective voltage, light-intensity dependent J_{SC} and V_{OC}, determination of the optical bandgap energy of NCBDT acceptor, EQE of EL measurements, dark current-density voltage curves, film absorption and quality comparison with THF and DCM solvents, absorption of PBDB-T film with and without DIM soaking, neutron reflectivity curves, field-dependent EL, field-dependent PL, transient absorption spectra, measurements on exciton diffusion length of PBDB-T, and device optimisation of sq-BHJ devices by varing the solvent for the acceptor layer, the spin speed of the acceptor layer and the donor layer.

Author Information

Corresponding Authors:

rhf10@cam.ac.uk;

yschen99@nankai.edu.cn;

ORCIDs

Jiangbin Zhang: 0000-0001-6565-5962

Andrew J. Parnell: 0000-0001-8606-8644

Xiao-Ke Liu: 0000-0001-5661-8174

Feng Gao: 0000-0002-2582-1740

Neil C. Greenham: 0000-0002-2155-2432

Yongsheng Chen: 0000-0003-1448-8177

Richard H. Friend: 0000-0001-6565-6308

Author Contributions:

[#]J.Z and B.K.: These authors contributed equally.

Acknowledgements:

We thank the Engineering and Physical Sciences Research Council for support. Experiments at the ISIS Pulsed Neutron and Muon Source were supported by a beamtime allocation (RB1800095) from the Science and Technology Facilities Council. We thank F. Auras, D. Credgington and S.M. Menke for helpful discussions. J. Z. thanks the China Scholarship Council for a PhD scholarship (No. 201503170255) and SPIE Optics and Photonics Education Scholarship. B.K., X.J.W. and Y.S.C. gratefully acknowledge the financial support from NSFC (91633301) and MoST (2014CB643502) of China. X.K.L. is a VINNMER and Marie Skłodowska Curie Fellow (No. 2016-02051). F.G. is a Wallenberg Academy Fellow. A.A.B. is a Royal Society University Research Fellow.

Table of Content Image

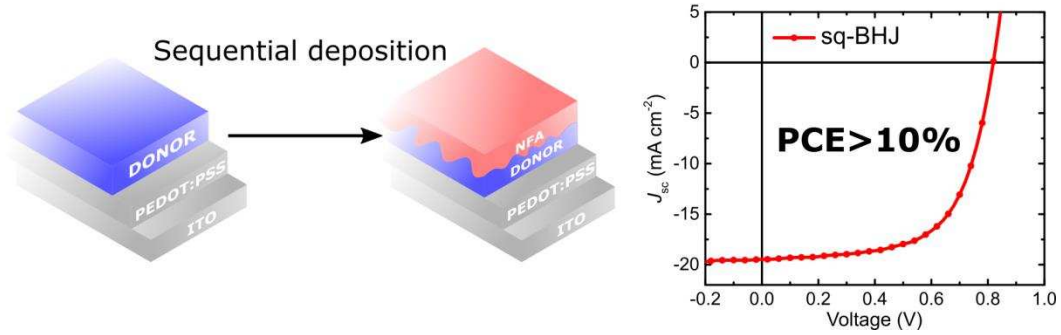
Sequential deposition
DONOR
PEDOT:PSS
ITO
NFA
DONOR
PEDOT:PSS
ITO
sq-BHJ
PCE>10%
J_{sc} (mA cm^{-2})
Voltage (V)
5
0
-5
-10
-15
-20
-0.2
0.0
0.2
0.4
0.6
0.8
1.0

Reference

(1) Li, G.; Zhu, R.; Yang, Y. Polymer Solar Cells. *Nat. Photonics* **2012**, *6* (3), 153–161.

(2) Heeger, A. J. 25th Anniversary Article: Bulk Heterojunction Solar Cells: Understanding the Mechanism of Operation. *Adv. Mater.* **2014**, *26* (1), 10–28.

(3) Tang, C. W. Two-Layer Organic Photovoltaic Cell. *Appl. Phys. Lett.* **1986**, *48* (2), 183–185.

(4) Yu, G.; Gao, J.; Hummelen, J. C.; Wudl, F.; Heeger, A. J. Polymer Photovoltaic Cells: Enhanced Efficiencies via a Network of Internal Donor-Acceptor Heterojunctions. *Science* **1995**, *270* (5243), 1789–1791.

(5) Halls, J. J. M.; Walsh, C. A.; Greenham, N. C.; Marseglia, E. A.; Friend, R. H.; Moratti, S. C.; Holmes, A. B. Efficient Photodiodes from Interpenetrating Polymer Networks. *Nature* **1995**, *376* (6540), 498–500.

(6) Zhao, F.; Wang, C.; Zhan, X. Morphology Control in Organic Solar Cells. *Adv. Energy Mater.* **2018**, *1703147*, 1–34.

(7) Frost, J. M.; Cheynis, F.; Tuladhar, S. M.; Nelson, J. Influence of Polymer-Blend Morphology on Charge Transport and Photocurrent Generation in Donor-Acceptor Polymer Blends. *Nano Lett.* **2006**, *6* (8), 1674–1681.

(8) Günes, S.; Neugebauer, H.; Sariciftci, N. S. Conjugated Polymer-Based Organic Solar Cells. *Chem. Rev.* **2007**, *107* (4), 1324–1338.

(9) Park, S. H.; Roy, A.; Beaupré, S.; Cho, S.; Coates, N.; Moon, J. S.; Moses, D.; Leclerc, M.; Lee, K.; Heeger, A. J. Bulk Heterojunction Solar Cells with Internal Quantum Efficiency Approaching 100%. *Nat. Photonics* **2009**, *3* (5), 297–302.

(10) Liu, Y.; Zhao, J.; Li, Z.; Mu, C.; Ma, W.; Hu, H.; Jiang, K.; Lin, H.; Ade, H.; Yan, H. Aggregation and Morphology Control Enables Multiple Cases of High-Efficiency Polymer Solar Cells. *Nat. Commun.* **2014**, *5*, 5293.

(11) Deng, D.; Zhang, Y.; Zhang, J.; Wang, Z.; Zhu, L.; Fang, J.; Xia, B.; Wang, Z.; Lu, K.; Ma, W.; et al. Fluorination-Enabled Optimal Morphology Leads to over 11% Efficiency for Inverted Small-Molecule Organic Solar Cells. *Nat. Commun.* **2016**, *7*, 13740.

(12) Zhao, J.; Li, Y.; Yang, G.; Jiang, K.; Lin, H.; Ade, H.; Ma, W.; Yan, H. Efficient Organic Solar Cells Processed from Hydrocarbon Solvents. *Nat. Energy* **2016**, *1* (2), 15027.

(13) Scharber, M. C.; Mühlbacher, D.; Koppe, M.; Denk, P.; Waldauf, C.; Heeger, A. J.; Brabec, C. J. Design Rules for Donors in Bulk-Heterojunction Solar Cells - Towards 10 % Energy-Conversion Efficiency. *Adv. Mater.* **2006**, *18* (6), 789–794.

(14) Brédas, J. L.; Norton, J. E.; Cornil, J.; Coropceanu, V. Molecular Understanding of Organic Solar Cells: The Challenges. *Acc. Chem. Res.* **2009**, *42* (11), 1691–1699.

(15) Hoppe, H.; Niggemann, M.; Winder, C.; Kraut, J.; Hiesgen, R.; Hinsch, A.; Meissner, D.; Sariciftci, N. S. Nanoscale Morphology of Conjugated Polymer/Fullerene-Based Bulk- Heterojunction Solar Cells. *Adv. Funct. Mater.* **2004**, *14* (10), 1005–1011.

(16) Ye, L.; Hu, H.; Ghasemi, M.; Wang, T.; Collins, B. A.; Kim, J. H.; Jiang, K.; Carpenter, J. H.; Li, H.; Li, Z.; et al. Quantitative Relations between Interaction Parameter, Miscibility and Function in Organic Solar Cells. *Nat. Mater.* **2018**, *17* (3), 253–260.

(17) Cheng, P.; Yan, C.; Wu, Y.; Dai, S.; Ma, W.; Zhan, X. Efficient and Stable Organic Solar Cells via a Sequential Process. *J. Mater. Chem. C* **2016**, *4* (34), 8086–8093.

(18) Seok, J.; Shin, T. J.; Park, S.; Cho, C.; Lee, J. Y.; Ryu, D. Y.; Kim, M. H.; Kim, K. Efficient Organic Photovoltaics Utilizing Nanoscale Heterojunctions in Sequentially Deposited Polymer/Fullerene Bilayer. *Sci. Rep.* **2015**, *5*, 8373.

(19) Van Franeker, J. J.; Kouijzer, S.; Lou, X.; Turbiez, M.; Wienk, M. M.; Janssen, R. A. J. Depositing Fullerenes in Swollen Polymer Layers via Sequential Processing of Organic Solar Cells. *Adv. Energy Mater.* **2015**, *5* (14), 1500464.

(20) Aguirre, J. C.; Hawks, S. A.; Ferreira, A. S.; Yee, P.; Subramaniyan, S.; Jenekhe, S. A.; Tolbert, S. H.; Schwartz, B. J. Sequential Processing for Organic Photovoltaics: Design Rules for Morphology Control by Tailored Semi-Orthogonal Solvent Blends. *Adv. Energy Mater.* **2015**, *5* (11), 1402020.

(21) Cheng, P.; Hou, J.; Li, Y.; Zhan, X. Layer-by-Layer Solution-Processed Low-Bandgap Polymer-PC61BM Solar Cells with High Efficiency. *Adv. Energy Mater.* **2014**, *4* (9), 1–7.

(22) Wang, D. H.; Moon, J. S.; Seifter, J.; Jo, J.; Park, J. H.; Park, O. O.; Heeger, A. J. Sequential Processing: Control of Nanomorphology in Bulk Heterojunction Solar Cells. *Nano Lett.* **2011**, *11* (8), 3163–3168.

(23) Moon, J. S.; Takacs, C. J.; Sun, Y.; Heeger, A. J. Spontaneous Formation of Bulk Heterojunction Nanostructures: Multiple Routes to Equivalent Morphologies. *Nano Lett.* **2011**, *11* (3), 1036–1039.

(24) Yan, Y.; Liu, X.; Wang, T. Conjugated-Polymer Blends for Organic Photovoltaics: Rational Control of Vertical Stratification for High Performance. *Adv. Mater.* **2017**, *29* (20), 1601674.

(25) Nakano, K.; Tajima, K. Organic Planar Heterojunctions: From Models for Interfaces in Bulk Heterojunctions to High-Performance Solar Cells. *Adv. Mater.* **2017**, *29* (25), 1603269.

(26) Inaba, S.; Vohra, V. Fabrication Processes to Generate Concentration Gradients in Polymer Solar Cell Active Layers. *Materials (Basel).* **2017**, *10* (5), 518.

(27) Chen, D.; Liu, F.; Wang, C.; Nakahara, A.; Russell, T. P. Bulk Heterojunction Photovoltaic Active Layers via Bilayer Interdiffusion. *Nano Lett.* **2011**, *11* (5), 2071–2078.

(28) Huang, L.; Wang, G.; Zhou, W.; Fu, B.; Cheng, X.; Zhang, L.; Yuan, Z.; Xiong, S.; Zhang, L.; Xie, Y.; et al. Vertical Stratification Engineering for Organic Bulk-Heterojunction Devices. *ACS Nano* **2018**, *12* (5), 4440–4452.

(29) Jang, Y.; Ju Cho, Y.; Kim, M.; Seok, J.; Ahn, H.; Kim, K. Formation of Thermally Stable Bulk Heterojunction by Reducing the Polymer and Fullerene Intermixing. *Sci. Rep.* **2017**, *7* (1), 9690.

(30) Hwang, H.; Lee, H.; Shafian, S.; Lee, W.; Seok, J.; Ryu, K.; Yeol Ryu, D.; Kim, K. Thermally Stable Bulk Heterojunction Prepared by Sequential Deposition of Nanostructured Polymer and Fullerene. *Polymers (Basel).* **2017**, *9* (9), 456.

(31) Yan, C.; Barlow, S.; Wang, Z.; Yan, H.; Jen, A. K. Y.; Marder, S. R.; Zhan, X. Non-Fullerene Acceptors for Organic Solar Cells. *Nat. Rev. Mater.* **2018**, *3*, 1–19.

(32) Hou, J.; Inganäs, O.; Friend, R. H.; Gao, F. Organic Solar Cells Based on Non-Fullerene Acceptors. *Nat. Mater.* **2018**, *17* (2), 119–128.

(33) Cheng, P.; Li, G.; Zhan, X.; Yang, Y. Next-Generation Organic Photovoltaics Based on Non-Fullerene Acceptors. *Nat. Photonics* **2018**, *12* (3), 131–142.

(34) Li, Z.; Jiang, K.; Yang, G.; Lai, J. Y. L.; Ma, T.; Zhao, J.; Ma, W.; Yan, H. Donor Polymer Design Enables Efficient Non-Fullerene Organic Solar Cells. *Nat. Commun.* **2016**, *7*, 13094.

(35) Lin, Y.; Wang, J.; Zhang, Z.; Bai, H.; Li, Y.; Zhu, D.; Zhan, X. An Electron Acceptor Challenging Fullerenes for Efficient Polymer Solar Cells. *Adv. Mater.* **2015**, *27* (7), 1170–1174.

(36) Zhao, W.; Li, S.; Yao, H.; Zhang, S.; Zhang, Y.; Yang, B.; Hou, J. Molecular Optimization Enables over 13% Efficiency in Organic Solar Cells. *J. Am. Chem. Soc.* **2017**, *139* (21), 7148–7151.

(37) Bin, H.; Gao, L.; Zhang, Z. G.; Yang, Y.; Zhang, Y.; Zhang, C.; Chen, S.; Xue, L.; Yang, C.; Xiao, M.; et al. 11.4% Efficiency Non-Fullerene Polymer Solar Cells with Trialkylsilyl Substituted 2D-Conjugated Polymer as Donor. *Nat. Commun.* **2016**, *7*, 13651.

(38) Zhang, G.; Yang, G.; Yan, H.; Kim, J. H.; Ade, H.; Wu, W.; Xu, X.; Duan, Y.; Peng, Q. Efficient Nonfullerene Polymer Solar Cells Enabled by a Novel Wide Bandgap Small Molecular Acceptor. *Adv. Mater.* **2017**, *29* (18), 1606054.

(39) Chen, S.; Liu, Y.; Zhang, L.; Chow, P. C. Y.; Wang, Z.; Zhang, G.; Ma, W.; Yan, H. A Wide-Bandgap Donor Polymer for Highly Efficient Non-Fullerene Organic Solar Cells with a Small Voltage Loss. *J. Am. Chem. Soc.* **2017**, *139* (18), 6298–6301.

(40) Holliday, S.; Ashraf, R. S.; Wadsworth, A.; Baran, D.; Yousaf, S. A.; Nielsen, C. B.; Tan, C.-H.; Dimitrov, S. D.; Shang, Z.; Gasparini, N.; et al. High-Efficiency and Air-Stable P3HT-Based Polymer Solar Cells with a New Non-Fullerene Acceptor. *Nat. Commun.* **2016**, *7*, 11585.

(41) Zhang, S.; Qin, Y.; Zhu, J.; Hou, J. Over 14% Efficiency in Polymer Solar Cells Enabled by a Chlorinated Polymer Donor. *Adv. Mater.* **2018**, *30* (20), 1800868.

(42) Sun, J.; Ma, X.; Zhang, Z.; Yu, J.; Zhou, J.; Yin, X.; Yang, L.; Geng, R.; Zhu, R.; Zhang, F.; et al. Dithieno[3,2- *b* :2′,3′- *d*]Pyrrol Fused Nonfullerene Acceptors Enabling Over 13% Efficiency for Organic Solar Cells. *Adv. Mater.* **2018**, *30* (16),

1707150.

(43) Fei, Z.; Eisner, F. D.; Jiao, X.; Azzouzi, M.; Röhr, J. A.; Han, Y.; Shahid, M.; Chesman, A. S. R.; Easton, C. D.; McNeill, C. R.; et al. An Alkylated Indacenodithieno[3,2- *b*]Thiophene-Based Nonfullerene Acceptor with High Crystallinity Exhibiting Single Junction Solar Cell Efficiencies Greater than 13% with Low Voltage Losses. *Adv. Mater.* **2018**, *30* (8), 1705209.

(44) Li, S.; Ye, L.; Zhao, W.; Yan, H.; Yang, B.; Liu, D.; Li, W.; Ade, H.; Hou, J. A Wide Band-Gap Polymer with a Deep HOMO Level Enables 14.2% Efficiency in Polymer Solar Cells. *J. Am. Chem. Soc.* **2018**, *140* (23), 7159–7167.

(45) Baran, D.; Gasparini, N.; Wadsworth, A.; Tan, C. H.; Wehbe, N.; Song, X.; Hamid, Z.; Zhang, W.; Neophytou, M.; Kirchartz, T.; et al. Robust Nonfullerene Solar Cells Approaching Unity External Quantum Efficiency Enabled by Suppression of Geminate Recombination. *Nat. Commun.* **2018**, *9* (1), 2059.

(46) Xu, X.; Bi, Z.; Ma, W.; Wang, Z.; Choy, W. C. H.; Wu, W.; Zhang, G.; Li, Y.; Peng, Q. Highly Efficient Ternary-Blend Polymer Solar Cells Enabled by a Nonfullerene Acceptor and Two Polymer Donors with a Broad Composition Tolerance. *Adv. Mater.* **2017**, *29* (46), 1704271.

(47) Zhang, G.; Zhang, K.; Yin, Q.; Jiang, X.-F.; Wang, Z.; Xin, J.; Ma, W.; Yan, H.; Huang, F.; Cao, Y. High-Performance Ternary Organic Solar Cell Enabled by a Thick Active Layer Containing a Liquid Crystalline Small Molecule Donor. *J. Am. Chem. Soc.* **2017**, *139* (6), 2387–2395.

(48) Baran, D.; Ashraf, R. S.; Hanifi, D. A.; Abdelsamie, M.; Gasparini, N.; Röhr, J. A.; Holliday, S.; Wadsworth, A.; Lockett, S.; Neophytou, M.; et al. Reducing the Efficiency–stability–cost Gap of Organic Photovoltaics with Highly Efficient and Stable Small Molecule Acceptor Ternary Solar Cells. *Nat. Mater.* **2017**, *16* (3), 363–369.

(49) Wang, Z.; Zhu, X.; Zhang, J.; Lu, K.; Fang, J.; Zhang, Y.; Wang, Z.; Zhu, L.; Ma, W.; Shuai, Z.; et al. From Alloy-Like to Cascade Blended Structure: Designing High-Performance All-Small-Molecule Ternary Solar Cells. *J. Am. Chem. Soc.* **2018**, *140* (4), 1549–1556.

(50) Cui, Y.; Yao, H.; Gao, B.; Qin, Y.; Zhang, S.; Yang, B.; He, C.; Xu, B.; Hou, J. Fine-Tuned Photoactive and Interconnection Layers for Achieving over 13% Efficiency in a Fullerene-Free Tandem Organic Solar Cell. *J. Am. Chem. Soc.* **2017**, *139* (21), 7302–7309.

(51) Zuo, L.; Yu, J.; Shi, X.; Lin, F.; Tang, W.; Jen, A. K.-Y. High-Efficiency Nonfullerene Organic Solar Cells with a Parallel Tandem Configuration. *Adv. Mater.* **2017**, *29* (34), 1702547.

(52) Cui, Y.; Yao, H.; Yang, C.; Yang, S.; Hou, J. Organic Solar Cells with an Efficiency Approaching 15%. *Acta Polym. Sin.* **2018**, No. 2.

(53) Zhang, Y.; Kan, B.; Sun, Y.; Wang, Y.; Xia, R.; Ke, X.; Yi, Y.-Q.-Q.; Li, C.; Yip, H.-L.; Wan, X.; et al. Nonfullerene Tandem Organic Solar Cells with High Performance of 14.11%. *Adv. Mater.* **2018**, *30* (18), 1707508.

(54) Li, Y.; Lin, J.-D.; Che, X.; Qu, Y.; Liu, F.; Liao, L.-S.; Forrest, S. R. High Efficiency Near-Infrared and Semitransparent Non-Fullerene Acceptor Organic Photovoltaic Cells. *J. Am. Chem. Soc.* **2017**, *139* (47), 17114–17119.

(55) Cui, Y.; Yang, C.; Yao, H.; Zhu, J.; Wang, Y.; Jia, G.; Gao, F.; Hou, J. Efficient Semitransparent Organic Solar Cells with Tunable Color Enabled by an Ultralow-Bandgap Nonfullerene Acceptor. *Adv. Mater.* **2017**, *29* (43), 1703080.

(56) Dai, S.; Zhan, X. Nonfullerene Acceptors for Semitransparent Organic Solar Cells. *Adv. Energy Mater.* **2018**, 1800002.

(57) Qian, D.; Ye, L.; Zhang, M.; Liang, Y.; Li, L.; Huang, Y.; Guo, X.; Zhang, S.; Tan, Z.; Hou, J. Design, Application, and Morphology Study of a New Photovoltaic Polymer with Strong Aggregation in Solution State. *Macromolecules* **2012**, *45* (24), 9611–9617.

(58) Yao, H.; Ye, L.; Zhang, H.; Li, S.; Zhang, S.; Hou, J. Molecular Design of Benzodithiophene-Based Organic Photovoltaic Materials. *Chem. Rev.* **2016**, *116* (12), 7397–7457.

(59) Kan, B.; Zhang, J.; Liu, F.; Wan, X.; Li, C.; Ke, X.; Wang, Y.; Feng, H.; Zhang, Y.; Long, G.; et al. Fine-Tuning the Energy Levels of a Nonfullerene Small-Molecule Acceptor to Achieve a High Short-Circuit Current and a Power Conversion Efficiency over 12% in Organic Solar Cells. *Adv. Mater.* **2018**, *30* (3), 1704904.

(60) Cui, Y.; Zhang, S.; Liang, N.; Kong, J.; Yang, C.; Yao, H.; Ma, L.; Hou, J. Toward Efficient Polymer Solar Cells Processed by a Solution-Processed Layer-By-Layer Approach. *Adv. Mater.* **2018**, 1802499.

(61) Harrison, M.; Grüner, J.; Spencer, G. Analysis of the Photocurrent Action Spectra of MEH-PPV Polymer Photodiodes. *Phys. Rev. B - Condens. Matter Mater. Phys.* **1997**, *55* (12), 7831–7849.

(62) Yao, J.; Kirchartz, T.; Vezie, M. S.; Faist, M. A.; Gong, W.; He, Z.; Wu, H.; Troughton, J.; Watson, T.; Bryant, D.; et al. Quantifying Losses in Open-Circuit Voltage in Solution-Processable Solar Cells. *Phys. Rev. Appl.* **2015**, *4* (1), 014020.

(63) Liu, J.; Chen, S.; Qian, D.; Gautam, B.; Yang, G.; Zhao, J.; Bergqvist, J.; Zhang, F.; Ma, W.; Ade, H.; et al. Fast Charge Separation in a Non-Fullerene Organic Solar Cell with a Small Driving Force. *Nat. Energy* **2016**, *1* (7), 16089.

(64) Dimitrov, S. D.; Bakulin, A. A.; Nielsen, C. B.; Schroeder, B. C.; Du, J.; Bronstein, H.; McCulloch, I.; Friend, R. H.; Durrant, J. R. On the Energetic Dependence of Charge Separation in Low-Band-Gap Polymer/Fullerene Blends. *J. Am. Chem. Soc.* **2012**, *134* (44), 18189–18192.

(65) Vandewal, K.; Benduhn, J.; Schellhammer, K. S.; Vangerven, T.; Rückert, J. E.; Piersimoni, F.; Scholz, R.; Zeika, O.; Fan, Y.; Barlow, S.; et al. Absorption Tails of Donor:C60 Blends Provide Insight into Thermally Activated Charge-Transfer Processes and Polaron Relaxation. *J. Am. Chem. Soc.* **2017**, *139* (4), 1699–1704.

(66) Benduhn, J.; Tvingstedt, K.; Piersimoni, F.; Ullbrich, S.; Fan, Y.; Tropiano, M.; McGarry, K. A.; Zeika, O.; Riede, M. K.; Douglas, C. J.; et al. Intrinsic Non-Radiative Voltage Losses in Fullerene-Based Organic Solar Cells. *Nat. Energy* **2017**, *2* (6).

(67) Vandewal, K.; Benduhn, J.; Nikolis, V. C. How to Determine Optical Gaps and Voltage Losses in Organic Photovoltaic Materials. *Sustain. Energy Fuels* **2017**, *2*, 538–544.

(68) Ran, N. A.; Love, J. A.; Takacs, C. J.; Sadhanala, A.; Beavers, J. K.; Collins, S. D.; Huang, Y.; Wang, M.; Friend, R. H.; Bazan, G. C.; et al. Harvesting the Full Potential of Photons with Organic Solar Cells. *Adv. Mater.* **2016**, *28* (7), 1482–1488.

(69) Yao, H.; Qian, D.; Zhang, H.; Qin, Y.; Xu, B.; Cui, Y.; Yu, R.; Gao, F.; Hou, J.

Critical Role of Molecular Electrostatic Potential on Charge Generation in Organic Solar Cells. *Chinese J. Chem.* **2018**, *36* (6), 491–494.

(70) Weu, A.; Hopper, T. R.; Lami, V.; Kreß, J. A.; Bakulin, A. A.; Vaynzof, Y. Field-Assisted Exciton Dissociation in Highly Efficient PffBT4T-2OD:Fullerene Organic Solar Cells. *Chem. Mater.* **2018**, *30* (8), 2660–2667.

(71) Menke, S. M.; Sadhanala, A.; Nikolka, M.; Ran, N. A.; Ravva, M. K.; Abdel-Azeim, S.; Stern, H. L.; Wang, M.; Sirringhaus, H.; Nguyen, T.-Q.; et al. Limits for Recombination in a Low Energy Loss Organic Heterojunction. *ACS Nano* **2016**, *10* (12), 10736–10744.

(72) Halls, J.; Pichler, K.; Friend, R.; Moratti, S.; Holmes, A. Exciton Dissociation at a Poly (p-Phenylenevinylene)/C 60 Heterojunction. *Synth. Met.* **1996**, *77*, 277–280.

(73) Stübinger, T.; Brütting, W. Exciton Diffusion and Optical Interference in Organic Donor-Acceptor Photovoltaic Cells. *J. Appl. Phys.* **2001**, *90* (7), 3632–3641.

(74) Névot, L.; Croce, P. Caractérisation Des Surfaces Par Réflexion Rasante de Rayons X. Application à l'étude Du Polissage de Quelques Verres Silicates. *Rev. Phys. Appliquée* **1980**, *15* (3), 761–779.